Pulsed Laser Annealing of Thin Films of Self-Assembled Nanocrystals

William J. Baumgardner,[†] Joshua J. Choi,[‡] Kaifu Bian,[§] Lena Fitting Kourkoutis,[‡] Detlef-M. Smilgies,[⊥] Michael O. Thompson,[∥] and Tobias Hanrath[§,*]

[†]Department of Chemistry and Chemical Biology, [‡]School of Applied and Engineering Physics, [§]School of Chemical and Biomolecular Engineering, [⊥]Cornell High Energy Synchrotron Source, and [∥]Department of Materials Science and Engineering, Cornell University, Ithaca, New York 14853, United States

ABSTRACT We investigated how pulsed laser annealing can be applied to process thin films of colloidal nanocrystals (NCs) into interconnected nanostructures. We illustrate the relationship between incident laser fluence and changes in morphology of PbSe NC films relative to bulk-like PbSe films. We found that laser pulse fluences in the range of 30 to 200 mJ/cm^2 create a processing window of opportunity where the NC film morphology goes through interesting transformations without large-scale coalescence of the NCs. NC coalescence can be mitigated by depositing a thin film of amorphous silicon (*a*-Si) on the NC film. Remarkably, pulsed laser annealing of the *a*-Si/PbSe NC films crystallized the silicon while NC morphology and translational order of the NC film are preserved.

KEYWORDS: nanocrystals · thin films · laser annealing · quantum confinement

Colloidal nanocrystals (NCs) are recognized as the elemental building blocks of emerging nanotechnologies. Recently, semiconductor NCs have garnered immense interest as material candidates for low-cost energy technologies including photovoltaics, photodetectors, thermoelectrics, and light-emitting diodes due to their solution processability combined with size- and shape-tunable optical and electrical properties.[1−8] While new NC materials continue to emerge, realization of the proposed NC-based technologies risks stalling in its rapid progress if unresolved challenges related to the processing of NCs into functional superstructures are not addressed.[9−15] A common requirement to bring their technological potential to fruition is to arrange NCs into functional structures in which the NCs are electrically coupled to each other and their surrounding environment. As-prepared colloidal NCs are typically coated with long-chain organic ligands that aid in dispersing the NCs and passivating their surfaces (Figure 1A). Unfortunately, this ligand shell also electrically isolates NCs from each other. Without surface stabilization, NCs are prone to sinter into mesoscopic aggregates and thus lose their nanoscale size-controlled properties. The fundamental challenge is therefore to balance the seemingly contradictory requirements of coupling NCs while preserving the effects of quantum confinement; the idealized confined-but-connected structure is illustrated in Figure 1B. A recent theoretical study by Sayle *et al.*[16] mapped out the rich diversity of nanostructures possible if controlled connections between NCs in periodic assemblies could be achieved. The lack of processing approaches to achieve such confined-but-connected nanostructures provides a strong motivation to investigate physical and chemical approaches to process NC assemblies.

Previous efforts to improve inter-NC connections include physical treatments (*e.g.*, thermal annealing[17,18] or plasma processing[19]) and chemical treatments (ligand exchange and displacement).[1,18,20,21] A critical drawback of thermal annealing is NC sintering, which leads to the loss of size-tuned properties. Chemical treatments effectively reduce the inter-NC separation, but typically disrupt the spatial coherence of the NC assembly leading to disordered films.[18,20−22] To preserve the nanostructured morphology and the order of the superstructure, the processing must be achieved with minimal diffusion of the constituent NCs. Nonequilibrium processes, such as rapid thermal annealing or pulsed laser annealing offer significant potential to decouple the diffusion dynamics from the physical processing. Laser annealing has already demonstrated numerous advantages in the fabrication of semiconductor thin films.[23] The prospect of applying laser annealing with rigorous control over the kinetics of NC melting, diffusion, and recrystallization is particularly attractive for the processing of NC assemblies and is the focus of this paper.

Pulsed laser annealing (PLA) utilizes a high intensity (0.3−30 MW/cm^2), but very brief laser pulse (3−30 ns) to irradiate the

* Address correspondence to th358@cornell.edu.

Received for review April 30, 2011 and accepted July 29, 2011.

Published online July 29, 2011
10.1021/nn201588p

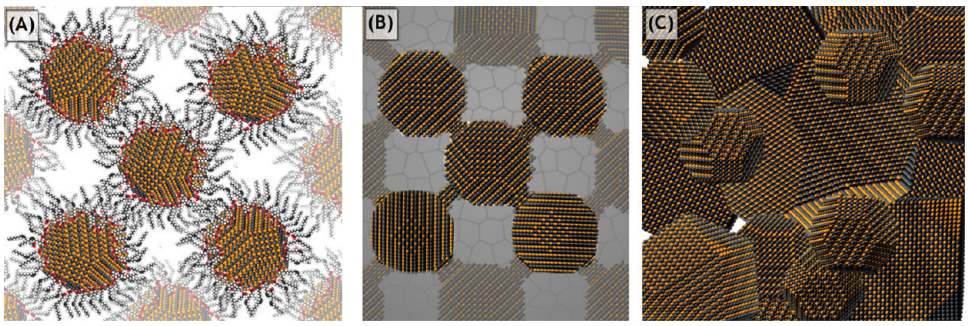

Figure 1. Schematic illustration of the balance between quantum-confinement and quantum-coupling. (A) Colloidal NCs passivated with organic ligands are strongly confined but largely isolated from one another. (B) Confined-but-connected structures that balance quantum confinement and coupling. (C) Complete coupling of the NCs in panel A leads to sintered polycrystalline structures.

sample, creating either a melting front that subsequently solidifies into a single or polycrystalline material, or thermal heating in solid phase on short time scales. The time scale for sample melting and resolidifying is typically submicrosecond.[24,25] The brief time in the molten state limits diffusion and enables the fabrication of unique and intricate structures.[26] Adjustments of the pulse duration and intensity introduce a high degree of tunability, including the ability to crystallize amorphous material and selectively anneal specific regions of a film.[24,27] The prospect of exploiting the tunability of PLA processing to create nanostructures with controlled morphologies is intriguing, but surprisingly the technique has been applied to nanomaterials only sparingly in the past, with some study of gold nanorods and nanoparticles, as well as synthesis of nanomaterials *via* ablation from the bulk.[28−31] Recently, laser annealing of an amorphous silicon/PbS NC solar cell device was shown to broaden the spectral response and increase external quantum efficiency, but detailed analysis of the structure was not reported.[32] Taking advantage of the uniquely short melt duration, we conjectured that it may be possible to anneal proximate NCs just enough that they become electronically coupled, while still preserving their quantum confinement as separate NCs. Furthermore, this process could be aided by embedding NCs in a matrix of a higher melting point material, allowing a small amount of flow between adjacent NCs while still being locked in their positions. Such films could have a transformative effect on NC device performance, but will require a systematic effort from the community to realize. This paper represents initial steps toward understanding the PLA process for NCs, in order to enable the fabrication of these and other film morphologies in the future.

Colloidal lead-salt (PbX; X = S, Se) NCs provide an ideal experimental platform for the study of confined-but-connected nanostructures processed by PLA. Established synthesis methods offer robust control over NCs with well-defined size, shape, and crystal structure. The large diameter of the Bohr exciton leads to efficient quantum mechanical coupling between proximate NCs[20] and sets the stage for creating metamaterials in which emerging optical and electrical properties can be controlled by adjusting the physical and electrical coupling between NCs in the superstructure. Previous NC syntheses[33,34] and recent *in situ* transmission electron microscopy (TEM)[35] showed that PbSe NCs can fuse at temperatures far below their melting points. These observations present a strong motivation to investigate whether such NC fusion processes can be controlled and directed during the processing of NC thin films. To establish the appropriate controls, we start our investigation by comparing laser annealing of NC thin films with those of a "bulk" PbSe film. This provides comparison for NC melt conditions, giving insight into the annealing process and allowing for better understanding of the evolution of crystal structure and morphology of NC films under a variety of annealing scenarios. We probed the structure of annealed films using electron microscopy and X-ray scattering. Additionally, we illustrate PLA on nanocomposites comprised of amorphous silicon layers sputter deposited onto a PbSe NC assembly.

RESULTS AND DISCUSSION

To understand how the nanostructured morphology influences the laser-annealing threshold, we compared a thin film of bulk PbSe crystal and colloidal PbSe NC films. We irradiated a 900 nm thick PbSe crystal grown *via* molecular beam epitaxy with ⟨111⟩ orientation on a BaF_2 substrate.[36] We adjusted the laser pulse energy density in the range of 10−500 mJ/cm^2 and monitored the reflectance of the film using a 650 nm laser diode and photodetector. Time-resolved reflectance measurements exhibit two distinct features. First, the spike in reflectance immediately following the laser pulse is characteristic of the transient melt of a semiconductor, as their liquids are typically metallic.[25,37−39] Second, long-term (after 1 μs) changes in the reflectance baseline indicate a permanent change in film reflectance arising from either modifications in the electronic structure or the morphology of the film.

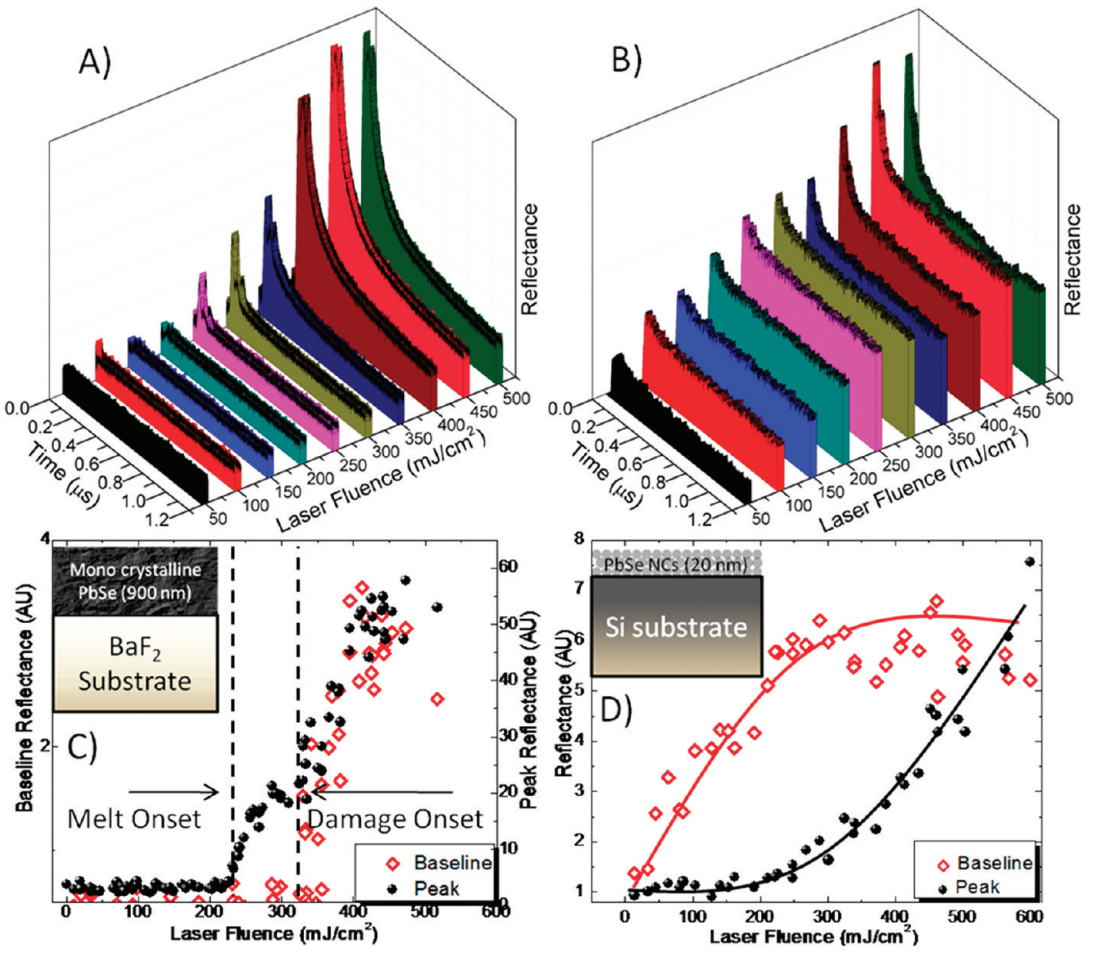

Figure 2. Reflectance data for a variety of different laser shots on both bulk PbSe and PbSe_OA NCs. (A) Reflectance *versus* time traces for bulk PbSe at a variety of different laser fluences. (B) Reflectance *versus* time traces for a thin layer of spin-casted PbSe_OA NCs. (C) Baseline and peak reflectance characteristics for bulk PbSe at a range of laser fluences. Peak reflectance is defined as the maximum reflectance minus the postannealing baseline. The method for baseline subtraction is described in the Supporting Information. (inset) Schematic of the bulk PbSe sample. (D) Baseline and peak reflectance characteristics for PbSe_OA NCs at a range of laser fluences. The curves are presented as a guide to the eye and do not represent any statistical or theoretical model. (inset) Schematic of PbSe_OA sample.

Figure 2A shows the time-resolved reflectance for bulk PbSe films as a function of the incident pulsed laser fluence. Figure 2C illustrates how the peak reflectance (defined as the maximum reflectance minus the postannealing baseline) varies under the same conditions. The melt transition is marked by a sudden increase in peak reflectance. In the case of bulk PbSe crystal, the apparent melt onset occurred near 220 mJ/cm^2. The change in baseline reflectance after the laser pulse as a function of incident laser fluence is also presented. The baseline remains essentially constant at laser fluences below 350 mJ/cm^2, at which point both the baseline and peak reflectance rapidly increase. This behavior, combined with visual changes to the film's appearance were consistent with the onset of damage (material ablation, macroscopic inhomogeneities, *etc.*). Taken together, these threshold studies suggest that laser pulses in the range of 220−350 mJ/cm^2 can melt the PbSe crystal without causing permanent changes in the film.

In contrast to the well-defined melting threshold observed in the bulk PbSe crystal, PbSe NC films exhibit a more gradual evolution of the peak reflectance with increasing laser fluence starting at about 200 mJ/cm^2 (Figure 2D). The magnitude of the melting signal is much smaller than for the bulk sample; we attribute the reduced melting signal to the difference in film thicknesses (20−25 nm *vs* 900 nm). Analysis of the post annealing reflectance baseline (Figure 2D) shows a gradual increase beginning with very small laser fluence (30 mJ/cm^2) which saturates above approximately 250 mJ/cm^2. The trends in short- and long-term reflectance lead to the encouraging conclusion that the laser pulses with fluence ranging from 30 to 200 mJ/cm^2 provide a window of opportunity to induce permanent changes in the NC film morphology without actually melting the NCs. We note that these observations are consistent with recent reports by van Huis *et al.* in which *in situ* TEM experiments observe NC fusion at temperatures well below the melt

threshold.[35] The melt duration of the NCs, defined as the full width half-maximum of the melt peak was consistently about 20 ns, further supporting the case for limited diffusion. Changes in the morphology of the NC film are likely sensitive to a complex set of parameters including the reduced melting point of isolated NCs, the initial separation between NCs and the extent of order within the film, as well as the film thickness and related vertical gradients arising from the transient laser heating and cooling.

Colloidal NC systems are known to melt at significantly lower temperatures than their bulk counterparts.[40−42] We investigated phase transitions of colloidal PbSe NC films *via* differential scanning calorimetry (DSC). Owing to instrumental constraints of the DSC to temperatures below 600 °C, this study was limited to small (diameter ~1.9 nm) NCs with pronounced reduction of melting point. The first DSC scan shows two prominent features: first a pronounced transition near 355 °C, which we attribute to the evaporation of oleic acid ligands. A second broad transition near 450 °C (Supporting Information, Figure S1) is attributed to the melting of the PbSe NC core. The magnitude of the melting point reduction is consistent with related theoretical and experimental studies which showed that the melting point of compound semiconductors is expected to vary inversely with $(1/d)^2$, where d is the particle diameter.[41] Given the melting point of the small diameter PbSe NCs, bulk PbSe as reference points, and the $1/d^2$ scaling relation,[41] we can roughly approximate the melting point of the 4.5 nm PbSe NCs used in the PLA studies to be in the range of 950−1000 °C.

The extent to which proximate NCs fuse during PLA processing should be sensitive to the initial separation between NCs, their order in the film and the thickness of the film. To investigate these parameters we compared NC films formed from oleic acid passivated NCs to films subjected to ligand exchange by ethanedithiol (EDT) treatment. The EDT ligand treatment significantly alters the structure of the NC film including a substantial reduction in inter-NC separation[21] as well as a loss of long-range translational order.[22,43] We will refer to NC films with oleic acid or ethanedithiol ligands as PbSe_OA and PbSe_EDT, respectively. To simulate NC film conditions encountered in device studies,[1] we limit the study here to film thicknesses below 100 nm. In thicker films, vertical gradients in the melting and recrystallization are likely to obscure the direct comparison. Additional experiments and theoretical investigation are required to understand melting and recrystallization dynamics in thicker NC films in which extremely low thermal conductivities may impact laser melt dynamics.[6,44−47] In particular, more study is needed to understand how the annealing process varies as a function of film depth in thicker samples (Supporting Information, Figure S2).

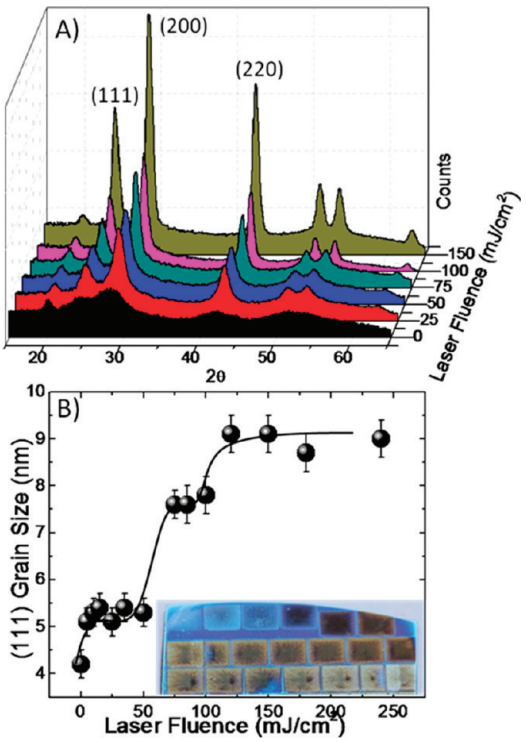

Figure 3. (A) X-ray diffraction of PbSe_EDT NCs annealed at various fluences. (B) Plot of the grain size as determined by Scherrer analysis of the ⟨111⟩ reflection *versus* laser fluence. The curve does not represent any statistical or theoretical model. (Inset) Photograph of a PbSe_EDT sample annealed at various laser fluences, increasing in power from the top left to the bottom right.

The laser annealing threshold of PbSe_EDT films differs significantly from the PbSe_OA NC films discussed above. The maximum and baseline reflectance rise as laser fluence increases (Supporting Information, Figure S3). Unlike PbSe_OA films, we cannot discern a minimum fluence required to induce permanent structural changes in the PbSe_EDT NC film; even very low fluences (<30 mJ/cm^2) induce permanent changes in the baseline reflectance. Furthermore, in contrast to the oleic acid-capped samples, a melt signal threshold could not be directly correlated to laser fluence since the transient melt signal is obscured by the rougher film morphology. These data indicate that the initial NC spacing and film thickness significantly impact the response to PLA. The complex trends in film reflectance with increasing laser fluence are likely the result of vertical variations in the melting and recrystallization behavior; further studies to elucidate this effect are currently underway.

To obtain more information about the crystallographic nature of the annealed NC films, we turned to X-ray diffraction (XRD). For this study, we focused on PbSe_EDT NC films since the layer-by-layer deposition enabled the formation of crack-free films with appropriate thickness required to obtain sufficient signal-to-noise in the diffractogram. Separate regions of the same NC film were illuminated with different laser

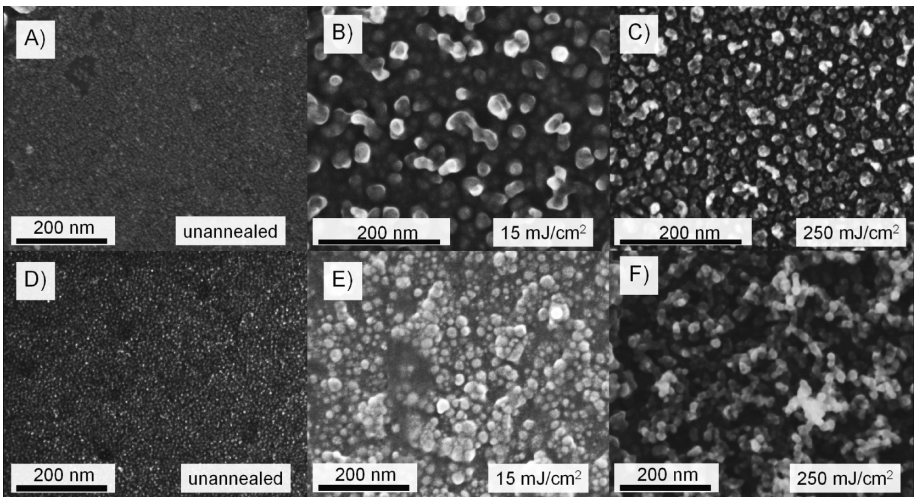

Figure 4. Scanning electron micrographs of NC films. (A) Unannealed, single-spin-coated layer of PbSe_OA NCs, about 20 nm thick. (B) Film A after laser annealing at 14 mJ/cm^2. (C) Film A after laser annealing at 248 mJ/cm^2. (D) Unannealed, layer by layer deposited PbSe_EDT NCs, about 50 nm thick. (E) Film D after laser annealing at 13 mJ/cm^2. (F) Film D after annealing at 241 mJ/cm^2.

fluences (Figure 3A) and then probed using a general area diffraction detector system. From the diffraction data, it is apparent that even at 5 mJ/cm^2 laser fluence there is a narrowing of each of the characteristic reflections, indicative of a grain size increase (Figure 3B). Correlated with the results from the reflectance analysis, we can conclude that this is not due to a substantial amount of NC melting (Figure 2), but rather due to a permanent change in the morphological structure and organization of the NC film. Three discrete regimes of grain size increase are observed: from 5 to 50 mJ/cm^2, 75−100 mJ/cm^2, and above 125 mJ/cm^2. Beyond 125 mJ/cm^2 there is an increase in grain size to about 9 nm, a little over twice the original NC size (4.3 nm). Further increase in laser power to 250 mJ/cm^2 did not significantly increase the average crystal grain size. We attribute these discrete steps to the destruction of ligands causing short-range agglomeration of proximate NCs at low fluences, followed by local sintering at intermediate fluences and more complete sintering at high laser fluences. Since the NCs do not begin with orientational ordering, it is not expected that NC fusion will be wholly or mostly epitaxial. We interpret the asymptotic relationship between NC grain size and laser fluence above 125 mJ/cm^2 as an indication for the diffusion limitation to the coalescence of neighboring NCs. In other words, NCs appear to be restricted to fuse with NCs in their immediate vicinity, while diffusion to form larger aggregates is kinetically avoided due to the short duration of the laser pulse. By contrast, NC films subjected to conventional thermal annealing show grain sizes on the order of (40−50 nm) (Supporting Information, Figure S4)[18] and a high degree of oxidation.[48] The important conclusions emerging from this comparison is that PLA processing avoids the mesoscale sintering encountered in thermal annealing and chemical reactions with the environment.

We analyzed the NC films using scanning electron microscopy (SEM) to gain further insights into the morphological changes induced by PLA. The SEM images in Figure 4 compare the structures of PbSe_OA NC films and PbSe_EDT NC films. The direct comparison of the morphology changes in response to PLA illustrates the role of NC film thickness, ordering of NC within the film and the initial separation between NCs. PbSe_OA films exhibit hexagonal packing with a nearest neighbor spacing on the order of the length of the oleic acid ligand (∼1.8 nm); the PbSe_EDT films on the other hand are disordered with inter-NC separations typically less than a nanometer.[22]

The SEM images show that low fluence laser irradiation substantially changes the morphology of both PbSe_OA and PbSe_EDT NC films (Figure 4B,E). Laser annealing of the PbSe_OA NC film with a single 14 mJ/cm^2 shot converted the 5 nm particles into 20 nm nanostructures. Irradiating the same film with a single 248 mJ/cm^2 shot yielded a film with similar morphology, but with a somewhat smaller average size for the nanostructures (∼15 nm). The morphology of laser annealed PbSe_EDT NC films differs significantly from the PbSe_OA films. Low fluence irradiation led to a film of densely packed and disordered nanostructures with characteristic length scale of *ca.* 20−35 nm (Figure 4E). Higher fluence irradiation (241 mJ/cm^2) resulted in the formation of porous network structures (Figure 4F). X-ray scattering analysis reveals a grain size on the order of 9 nm which indicates that the ∼25 nm nano structures seen in the SEM images are multicrystalline. The images support our interpretation that grain size growth with higher laser fluence is not due to a

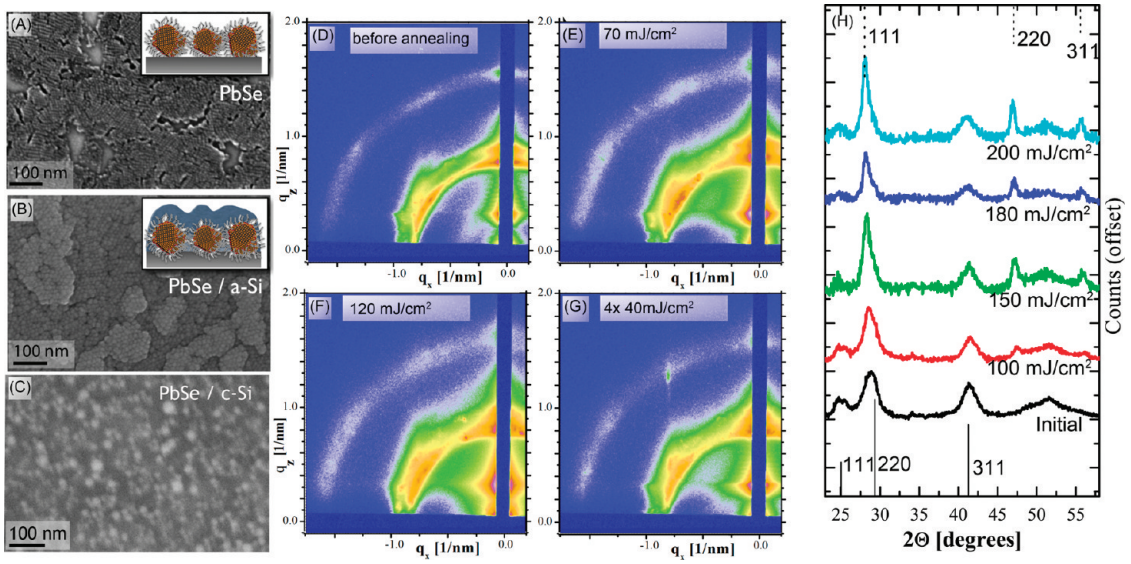

Figure 5. (A) Scanning electron microscopy image of a spin coated PbSe NC film. (B) Film A after sputter deposition of 100 nm *a*-Si. (C) Film B after laser annealing. Grazing incidence small-angle X-ray scattering of the PbSe/*a*-Si film after (D) no laser irradiation, (E) a 70 mJ/cm^2 pulse, (F) a 120 mJ/cm^2 pulse, (G) 4 pulses of 40 mJ/cm^2. (H) Wide angle X-ray scattering of the PbSe/*a*-Si film laser annealed at a variety of laser fluences. Literature reflections of Si and PbSe are marked by the dashed and solid lines, respectively. The emergence of the ⟨220⟩ and ⟨311⟩ Si peaks prove the crystallization of the amorphous layer.

substantial increase in feature size, but rather the annealing of grain boundaries within the agglomerated nanostructures. Pulsed laser annealing at high fluence (~250 mJ/cm^2) also led to the formation of micrometer long networked fibers. Additional SEM and TEM images of these structures, as well as microscale and intermediate annealing condition images, are shown in the Supporting Information (Figure S5). These structures likely form during the partial ablation of the PbSe_EDT NC film, although the underlying mechanism is presently still unknown.

Collectively, the structural analysis of PLA processed NC films shows that laser annealing leads to partial coalescence of the NCs in the film. Although the PLA treatment successfully avoids the formation of larger aggregates formed during conventional thermal annealing, we sought to refine the processing to further restrict NC coalescence and to preserve the ordering of NCs in the film. We conjectured that the introduction of a percolated inorganic matrix that is immiscible with the NC phase would create a unique system in which solid-phase kinetics are entirely suppressed (insufficient time) and immiscible liquid phase kinetics are severely restricted. In the specific example of PbSe NCs within a Si matrix, it may be possible to melt the NCs, while the percolated matrix remains solid, controlling diffusion of the particles and only allowing limited agglomeration. This approach was inspired by a recent work of Arora *et al.* who demonstrated that amorphous silicon deposited within porous templates can be laser annealed to yield single crystal Si structures.[26]

As a proof of concept for these ideas, we encapsulated PbSe_OA films by sputter depositing a thin layer (100 nm) of amorphous silicon (*a*-Si) on top of the NCs and annealing the composite film with a range of different laser fluences (Figure 5). We probed the nanostructure of the composite *a*-Si/PbSe films using synchrotron-based grazing incidence small-angle X-ray scattering (GISAXS). Small-angle scattering perpendicular to the substrate provides information about the ordering of NCs along the substrate normal and scattering parallel to the substrate surface yields information about the lateral ordering. Ring-like scattering features indicate a random polycrystalline orientation of NCs while well-defined scattering peaks indicate NC assemblies with specific orientations with respect to the substrate. An important advantage of GISAXS structure characterization is that it does not suffer from sampling bias like conventional imaging techniques, as it is an ensemble technique that gathers data from a relatively large region of the sample.

GISAXS patterns acquired at variable angles of incidence ranging from 0.05° to 0.45° confirm the layered structure of the *a*-Si/PbSe NC films (Supporting Information, Figure S6). Importantly, GISAXS analysis of the *a*-Si/PbSe films shows that the NCs retain a large degree of their translational ordering even after laser annealing (see Figure 5D-G). With increasing laser fluence, there is a significant reduction in superlattice *d*-spacing, likely caused by the partial loss of ligand coverage and the subsequent reduction of inter-NC spacing (Supporting Information, Figure S7). The grain

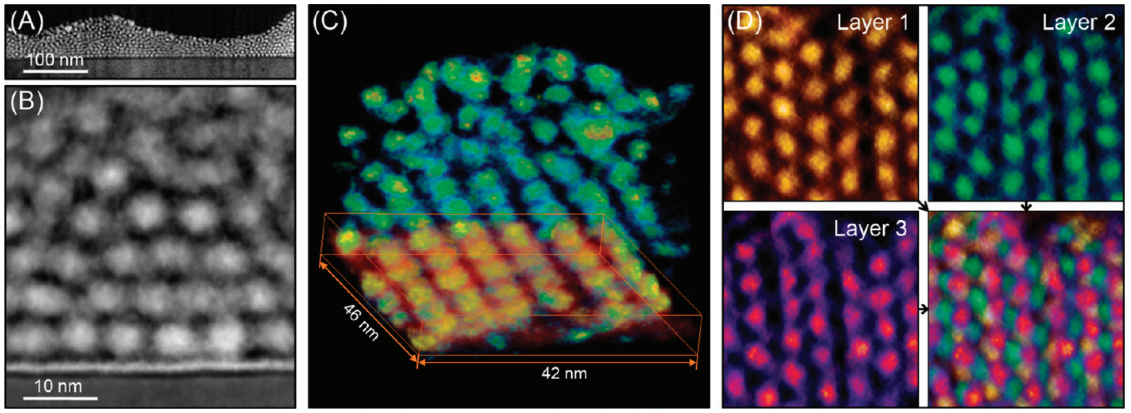

Figure 6. (A, B) Cross-sectional annular dark field scanning transmission electron microscopy images of a PbSe/*a*-Si nanocomposite film annealed by a 50 mJ/cm^2 laser pulse. (C) Tomographic reconstruction of the laser annealed nanocomposite film illustrating the three-dimensional (3D) arrangement of the NCs in the film. The 3D structure is shown by direct volume rendering of the reconstruction. The first NC layer is highlighted using a red-yellow-white color scale. (D) In plane ordering of the NCs in the first three layers of the film are shown as indicated in the individual panel.

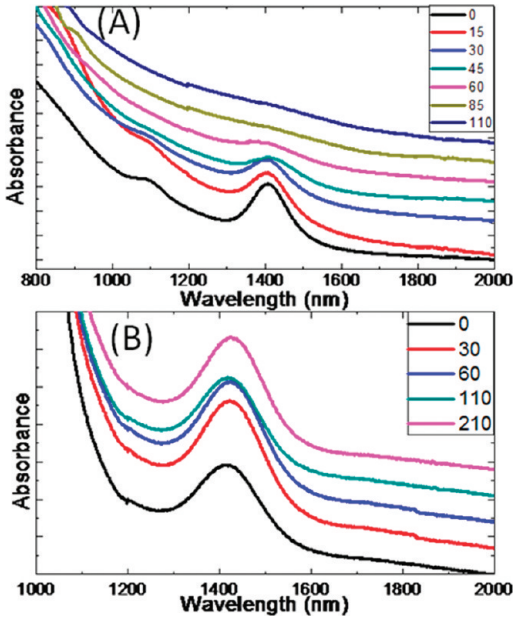

Figure 7. Ultraviolet−visible−near-infrared spectra of laser annealed (A) unencapsulated and (B) *a*-Si/PbSe_OA composite films. The large absorbance near 1400 nm is the excitonic peak of the NCs, while the trace labels are the laser power density for each trace in mJ/cm^2.

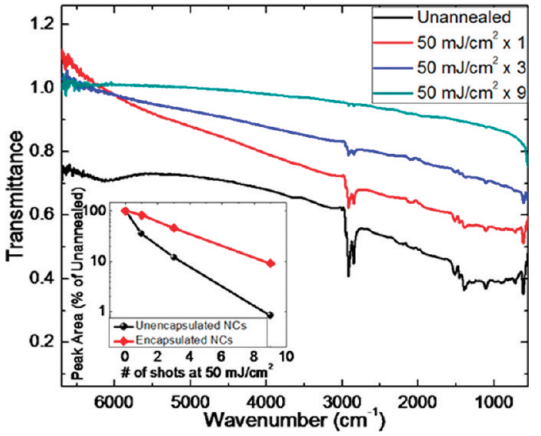

Figure 8. Fourier transform infrared spectroscopy of PbSe_OA NC films without an *a*-Si coating. Spectroscopy includes an unannealed region of the sample, as well as regions with varying amounts of 50 mJ/cm^2 shots. (Inset) Plot of integrated peak areas for the C−H stretch near 3000 wavenumbers presented as a percent of the unannealed peak area *vs* number of 50 mJ/cm^2 shots. PbSe_OA and *a*-Si/PbSe composite films are both presented.

size is also reduced by about 50%, but long-range ordering (superlattice grain size ~700 nm) is evident even in samples annealed at 120 mJ/cm^2. Remarkably, corresponding powder XRD patterns (Figure 5H) suggest that the PbSe NCs retain their original crystal size, while the emergence of the ⟨220⟩ and ⟨311⟩ silicon reflections show the crystallization of the *a*-Si. Cross-sectional scanning transmission electron microscopy (STEM) images showed that NCs within these films were partially coalesced but, importantly, retained much of their nanocrystalline character. (Figure 6, Supporting Information, Figure S8). Rather than the aggregation of particles into superstructures, the high-resolution micrographs evidence the partial fusion of NCs with their proximate neighbors. This provides the first hint of structures similar to the idealized confined-but-connected networks illustrated in Figure 1B. STEM tomography, which allows the 3-dimensional arrangement of the NCs in its network to be studied, confirmed that the ordering of the NCs is intact throughout much of the sample (Figure 6, Supporting Information, Figure S9). Near the top of the NC film, the ordering was less pronounced; this is either due to vertical variations in the laser induced restructuring or caused by the sputter deposition of the *a*-Si layer. To investigate the extent to which the sputter deposited silicon is integrated in the interstitial volume of the NC film, we analyzed the spatially resolved composition of the composite *a*-Si/PbSe NC film. Electron energy loss

spectroscopy of the film cross section shows that silicon is not present in the interstitial volume of the PbSe NC film which suggests that the silicon did not flow into the NC matrix under these conditions (Supporting Information, Figure S10). Instead, it appears that carbonaceous material is retained in the interstitial volume of the NC film. The ability of these heterosystems to control the particle aggregation and retain ordering while also forming crystalline inorganic/inorganic interfaces likely applies well beyond the studies here, and is useful for a wide variety of materials systems.

Optical measurements provide the most straightforward indication of optoelectronic coupling between NCs in connected superstructures. Optical absorption spectra of isolated PbSe NCs in solution are characterized by size-dependent excitonic signatures. A red-shift and broadening of the excitonic peak in NC films are attributed to changes in the polarization of the dielectric environment and changes in the electronic coupling.[43,49−51] A complete loss of excitonic spectral signatures is generally interpreted as an indication that NCs have sintered into a polycrystalline film. To study the extent of optoelectronic coupling in laser annealed PbSe NC films, we measured the optical absorption spectra of NC films processed under varying laser annealing conditions (Figure 7). We find that the evolution of the excitonic spectra in response to laser annealing depends critically on the presence of the sputter deposited a-Si layer. In the case of PbSe NC films without the a-Si, the excitonic peak survives low laser fluences (<50 mJ/cm^2) but is broadened sufficiently to be eliminated by 85 mJ/cm^2. By contrast, at each of the laser fluences measured (up to 210 mJ/cm^2) the excitonic peak signature remains prominent for composite *a*-Si/PbSe NC films, with a small amount of redshift and broadening as laser power increases. These findings suggest that PbSe_OA NC films are vulnerable to aggregation and loss of either monodispersity, quantum confinement, or both. Conversely, *a*-Si/PbSe NC composite films maintain a high degree of quantum confinement and monodispersity. Both of these findings are well supported by the XRD and microscopy data presented earlier.

One final consideration is the fate of the ligands during the annealing process. It is likely that many of the organics coating the particles are ablated, decomposed, or otherwise destroyed during the heating process. This supposition is supported by the X-ray, reflectance, and SEM data which show significant morphological changes despite minimal melting at low laser fluence. To examine this further, we probed the fate of the organics using Fourier transform infrared spectroscopy (FTIR) (Figure 8). By examining laser annealed PbSe_OA films, it is clear that the spectral signature of the organic ligand, most notably the C−H stretches near 3000 cm^{-1} diminish considerably with laser annealing. An approximate quantification of the ligand loss based on integration of the C−H peak area shows that for PbSe_OA NCs films, after one 50 mJ/cm^2 laser shot, the C−H stretches were diminished by an average of 58% per shot, indicating a substantial amount of ligand loss or decomposition. By coating the NCs in *a*-Si, an average of 17% of the C−H stretch was lost with each shot, proving that *a*-Si encapsulation significantly inhibits ligand degradation during the annealing process. This further explains why the *a*-Si/PbSe NC composite films have much less pronounced agglomeration despite the minimal flow of Si into the matrix. As expected, higher powers eliminate more ligands, though a fair amount survive even a 200 mJ/cm^2 pulse (Supporting Information, Figure S11). The excitonic peak, presenting near 6100 cm^{-1}, shows the same behavior as in the UV−vis−NIR spectra, broadening with a single 50 mJ/cm^2 shot and being eliminated by three. This data supports the notion that particle aggregation is caused at least partially by the destruction of ligands, while encapsulation is one method to control these effects.

CONCLUSIONS

We investigated how pulsed laser annealing can be applied to process colloidal films of PbSe NCs. We used reflectance measurements to determine the melt threshold of bulk and nanocrystalline PbSe films. Even at very low fluences (20 mJ/cm^2), permanent reflectance changes in response to PLA indicate structural changes in the NC film. Significant melting of the NC occurs at higher laser pulse fluences (>200 mJ/cm^2). XRD structural analysis revealed that PLA induces a small change in crystal grain size and seems to maximize around twice the original NC size. SEM structural characterization illustrated the porous, aggregated nature of laser annealed NC films, as well as the tendency for the particles to aggregate into one-dimensional strings. Much of the aggregation and disorder that is induced by the laser can be mitigated by adding a conformal layer of amorphous silicon on top of the film. At sufficiently intense laser fluences the silicon can be crystallized while translational ordering of PbSe NC in the underlying film is preserved. Characterization of the NC surface chemistry showed that the laser annealing process destroys many of the ligands coating the surface of the particles, but does so much less aggressively when they are encapsulated by sputter deposited *a*-Si. Collectively, our results illustrate how nonequilibrium processing, specifically pulsed laser annealing, can be applied to transform colloidal NC films into novel connected nanostructures. Further refinements of the processing conditions and exploration of other

NC core and matrix compositions are expected to yield a promising class of nanostructured confined-but-connected materials as a platform for exciting structure–property studies.

METHODS

Lead oxide (99.99%), selenium (99.999%, pellets), trioctylphosphine (90%, technical grade), 1-octadecene (90%, technical grade), oleic acid (90%, technical grade), hexamethyldisilathiane (synthesis grade), 1,2 ethanedithiol (90%, technical grade) were all purchased from Sigma-Aldrich and were used without purification. Common solvents such as hexanes and ethanol were purchased from various sources and used without purification. Bulk PbSe thin films were 900 nm and grown by molecular beam epitaxy on a ⟨111⟩ barium fluoride substrate. Prior to annealing, bulk PbSe films were soaked in a mild base bath in order to remove the thin native oxide layer.

Lead selenide NCs were synthesized using a modification of the method by Yu *et al.*[52] A typical synthesis is as follows: 0.90 g of PbO was mixed with 12.0 g of squalane and 2.9 g of oleic acid in a 3-neck flask and heated to 150 °C under nitrogen flow. The reactants are allowed to mix for 1 h until all of the PbO is dissolved. A 91 μL portion of diphenylphosphine was mixed with 12 mL of 1 M trioctylphosphine/selenide and rapidly injected into the lead/oleate solution. The mixture is allowed to heat back up to 150 °C and grow for 4 min until it is quenched. The product is rinsed with hexane and ethanol as solvent and antisolvent three times and stored dry in a nitrogen glovebox. Except for those used in DSC experiments, all PbSe NCs used in this experiment were 4–5 nm, with a size distribution under 10%.

PbSe_OA films were fabricated by spincoating 20 mg/mL PbSe NCs in chlorobenzene onto a clean Si substrate at 1000 rpm. PbSe_OA films were 20–25 nm thick. PbSe_EDT films were fabricated by spin coating 20 mg/mL PbSe NCs in chlorobenzene onto a clean substrate, then exposing the film to 0.1 M EDT in acetonitrile solution. The film was subsequently rinsed with acetonitrile and chlorobenzene. The process was repeated two more times for a total of three layers. PbSe_EDT films were 45–55 nm thick. All solutions used in film fabricated, including NC solutions, were filtered through a 0.45 μm filter prior to use. For encapsulated films, *a*-Si layer was deposited with CVC 601 sputter deposition system. RF magnetron source was used to reduce charge build-up. With source power at 2 kW and 10 mT of argon sputtering gas, the *a*-Si deposition rate was 87 Å/min. The deposition was done for 12 min to obtain ~100 nm thick *a*-Si film. The films used for UV–vis–NIR spectroscopy were similarly produced, but not the same that underwent STEM analysis.

Laser annealing was performed using a 308 nm Lambda Physik LPX205i XeCl eximer laser with a 30 ns pulse at full width half max, and a maximum pulse energy of 500 mJ. The beam is homogenized to 3.2 × 3.2 mm^2 square with fluences up to 1.5 J/cm^2. The time-resolved laser power is detailed in the Supporting Information (Figure S12). Reflectance was measured using a 650 nm diode laser monitored using an ORTEC FND-100Q detector connected to a Tektronix TDS 3054 500 MHz oscilloscope. Laser fluence was calibrated to the melt onset of ⟨100⟩ monocrystalline Si at 600 mJ/cm^2. Laser annealing is carried out in ambient atmosphere.

Wide angle XRD measurements are carried out using a Bruker General Area Detector Diffraction System with a 2-dimensional detector. Small angle X-ray measurements are carried out using the GISAXS setup at the Cornell High Energy Synchrotron Source (CHESS) (for details see ref 22). FTIR spectroscopy was performed using a Bruker Optics Vertex 80v spectrophotometer. UV–vis–NIR spectra were measured using a Varian Cary 5000 spectrophotometer operating in transmission mode with an air background. DSC was performed in a nitrogen environment using a TA Instruments DSC Q2000 instrument. SEM was performed on a Leo 1550 Field Emission SEM. Low resolution TEM images were obtained using an FEI T12 microscope operating at 120 kV. STEM imaging and tomography was performed on a 200 kV FEI Tecnai F20 SuperTWIN STEM equipped with a Gatan Tridiem 865ER imaging filter used for electron energy loss spectroscopy.

Acknowledgment. We thank Jan Koenig for providing bulk PbSe thin film samples. W.B. was supported by Award No. KUS-C1-018-02, made by King Abdullah University of Science and Technology (KAUST). K.B. was supported by NSF-CBET 0828703. J.J.C. was supported by the NSF IGERT Fellowship Program on "Nanoscale Control of Surfaces and Interfaces," administered by Cornell's MRSEC. We also acknowledge the Cornell Center for Materials Science (NSF DMR-0520404) and the Cornell High Energy Synchrotron Source (NSF DMR-09262384).

Supporting Information Available: Laser pulse output trace; additional SEM images, including low magnification and intermediate annealing conditions; Tomography analysis including the full 360 degree movie; FTIR analysis as a function of pulse energy. This material is available free of charge *via* the Internet at http://pubs.acs.org.

REFERENCES AND NOTES

1. Choi, J. J.; Lim, Y.-F.; Santiago-Berrios, M. E. B.; Oh, M.; Hyun, B.-R.; Sung, L.; Bartnik, A. C.; Goedhart, A.; Malliaras, G. G.; Abruna, H. D.; *et al.* PbSe Nanocrystal Excitonic Solar Cells. *Nano Lett.* **2009**, *9*, 3749–3755.
2. Gur, I.; Fromer, N. A.; Geier, M. L.; Alivisators, A. P. Air-Stable All-Inorganic Nanocrystal Solar Cells Processed from Solution. *Science* **2005**, *310*, 462–265.
3. Kamat, P. V. Quantum Dot Solar Cells. Semiconductor Nanocrystals as Light Harvesters. *J. Phys. Chem. C* **2008**, *112*, 18737–18753.
4. Konstantatos, G.; Levina, L.; Tang, J.; Sargent, E. H. Sensitive Solution-Processed Bi_2S_3 Nanocrystalline Photodetectors. *Nano Lett.* **2008**, *8*, 4002–4006.
5. Luther, J. M.; Law, M.; Beard, M. C.; Song, Q.; Reese, M. O.; Ellingson, R. J.; Nozik, A. J. Schottkey Solar Cells Based on Colloidal Nanocrystal Films. *Nano Lett.* **2008**, *8*, 3488–3492.
6. Wang, R. y.; Feser, J. P.; Lee, J.-S.; Talapin, D. V.; Segalman, R.; Majumdar, A. Enchanced Thermopower in PbSe Nanocrystal Quantum Dot Superlattices. *Nano Lett.* **2008**, *8*, 2283–2288.
7. Simon, J.; Jiaqing, H.; Androulakis, J.; Dravid, V. P.; Todorov, I.; Chung, D. Y.; Kanatzidis, M. G. Nanostructures Boost the Thermoelectric Performance of PbS. *J. Am. Chem. Soc.* **2011**, *133*, 3460–3470.
8. Achermann, M.; Petruska, M. A.; Koleske, D. D.; Crawford, M. H.; Klimov, V. I. Nanocrystal-Based Light-Emitting Diodes Utilizing High-Efficiency Nonradiative Energy Transfer for Color Conversion. *Nano Lett.* **2006**, *6*, 1396–1400.
9. Caldwell, M. A.; Raoux, S.; Wang, R. Y.; Wong, H.-S. P.; Milliron, D. J. Synthesis and Size-Dependent Crystallization of Colloidal Germanium Telluride Nanoparticles. *J. Mater. Chem.* **2010**, *20*, 1285–1291.
10. Ruddy, D. A.; Johnson, J. C.; Smith, E. R.; Neale, N. R. Size and Bandgap Control in the Solution-Phase Synthesis of Near-Infrared-Emitting Germanium Nanocrystals. *ACS Nano* **2010**, *4*, 7459–7466.
11. Mehta, R. J.; Karthik, C.; Jiang, E.; Singh, B.; Shi, Y.; Siegel, R. W.; Borca-Tasciuc, T.; Ramanath, G. High Electrical Conductivity Antimony Selenide Nanocrystals and Assemblies. *Nano Lett.* **2010**, *10*, 4417–4422.
12. Kruszynska, M.; Borchert, H.; Parisi, J.; Kolny-Olesiak, J. Synthesis and Shape Control and $CuInS_2$ Nanoparticles. *J. Am. Chem. Soc.* **2010**, *132*, 15976–15986.

13. Baumgardner, W. J.; Choi, J. J.; Lim, Y.-F.; Hanrath, T. SnSe Nanocrystals: Synthesis, Structure Optical Properties, and Surface Chemistry. *J. Am. Chem. Soc.* **2010**, *132*, 9519–9521.
14. Guo, Q.; Hillhouse, H. W.; Agrawal, R. Synthesis of Cu_2ZnSnS_4 Nanocrystal Ink and Its Use for Solar Cells. *J. Am. Chem. Soc.* **2009**, *131*, 11672–11673.
15. Shavel, A.; Arbiol, J.; Cabot, A. Synthesis of Quaternary Chalcogenide Nanocrystals: Stannite $Cu_2Zn_xSn_ySe_{1+x+2y}$. *J. Am. Chem. Soc.* **2010**, *132*, 4514–4515.
16. Sayle, D. C.; Seal, S.; Wang, Z.; Mangili, B. C.; Price, D. W.; Karakoti, A. S.; Kuchibhatla, S. T. V. N.; Hao, Q.; Mobus, G.; Xu, X.; *et al.* Mapping Nanostructure: A Systematic Enumeration of Nanomaterials by Assembling Nanobuilding Blocks at Crystallographic Positions. *ACS Nano* **2008**, *2*, 1237–1251.
17. Gur, I.; Fromer, N.; Geier, M.; Alivisatos, A. Air-Stable All-Inorganic Nanocrystal Solar Cells Processed from Solution. *Science* **2005**, *310*, 462–465.
18. Law, M.; Luther, J. M.; Song, O.; Hughes, B. K.; Perkins, C. L.; Nozik, A. J. Structural, Optical, and Electrical Properties of PbSe Nanocrystal Solids Treated Thermally or with Simple Amines. *J. Am. Chem. Soc.* **2008**, *130*, 5974–5985.
19. Cademartiri, L.; Ghadimi, A.; Ozin, G. A. Nanocrystal Plasma Polymerization: From Colloidal Nanocrystals to Inorganic Architectures. *Acc. Chem. Res.* **2008**, *41*), 1820–1830.
20. Talapin, D. V.; Murray, C. B. PbSe Nanocrystal Solids for *n*- and *p*-Channel Thin Film Field-Effect Transistors. *Science* **2005**, *310*, 86–89.
21. Luther, J.; Law, M.; Song, Q.; Perkins, C.; Beard, M.; Nozik, A. Structural, Optical, and Electrical Properties of Self-Assembled Films of PbSe Nanocrystals Treated with 1,2-Ethanedithiol. *ACS Nano* **2008**, *2*, 271–280.
22. Hanrath, T.; Choi, J. J.; Smilgies, D. Structure/Processing Relationships of Highly Ordered Lead Salt Nanocrystal Superlattices. *ACS Nano* **2009**, *3*, 2975–2988.
23. Ashfold, M.; Claeyssens, F.; Fuge, G.; Henley, S. Pulsed Laser Ablation and Deposition of Thin Films. *Chem. Soc. Rev.* **2004**, *33*, 23–31.
24. Wood, R. F.; Giles, G. E. Macroscopic Theory of Pulsed-Laser Annealing. 1. Thermal Transport and Melting. *Phys. Rev. B* **1981**, *23*, 2923–2942.
25. Auston, D. H.; Surko, C. M.; Venkatesan, T. N. C.; Slusher, R. E.; Golovchenko, J. A. Time-Resolved Reflectivity of Ion-Implanted Silicon During Laser Annealing. *Appl. Phys. Lett.* **1978**, *33*, 437–439.
26. Arora, H.; Du, P.; Tan, K. W.; Hyun, J. K.; Grazul, J.; Xin, H. L.; Muller, D. A.; Thompson, M. O.; Wiesner, U. Block Copolymer Self-Assembly-Directed Single-Crystal Homo- and Heteroepitaxial Nanostructure. *Science* **2010**, *330*, 214–218.
27. Stritzker, B.; Pospieszczyk, A.; Tagle, J. A. Measurement of Lattice Temperature of Silicon During Pulsed Laser Annealing. *Phys. Rev. Lett.* **1981**, *47*, 356–358.
28. Link, S.; Burda, C.; Nikoobakht, B.; El-Sayed, M. A. Laser Induced Shape Changes of Colloidal Gold Nanorods Using Femtosecond and Nanosecond Laser pulses. *J. Phys. Chem. B* **2000**, *104*, 6152–6163.
29. Mafune, F.; Kohno, J.-Y.; Takeda, Y.; Kondow, T. Formation of Gold Nanonetworks and Small Gold Nanoparticles by Irradiation of Intense Pulsed Laser onto Gold Nanoparticles. *J. Phys. Chem. B* **2003**, *107*, 12589–12596.
30. Wenzel, T.; Bosbach, J.; Goldmann, A.; Stietz, F.; Trager, F. Shaping Nanoparticles and Their Optical Spectra with Photons. *Appl. Phys. B-Lasers O.* **1999**, *69*, 513.
31. Bosbach, J.; Martin, D.; Stietz, F.; Wenzel, T.; Trager, F. Laser-Based Method for Fabricating Monodisperse Metallic Nanoparticles. *Appl. Phys. Lett.* **1999**, *74*, 2605–2607.
32. Mudugamuwa, N. K.; Dissanayake, D. M. N. M.; Adikaari, A. A. D. T.; Silva, S. R. P. Broadband Energy Harvesting with Nano-Composite PbS-Nanocrystal/Excimer Laser Crystallized Thin Film Silicon Hybrid Solar Cells. *Sol. Energ. Mat. Sol. C* **2009**, *93*, 549–551.
33. Cho, K.; Talapin, D.; Gaschler, W.; Murray, C. Designing PbSe Nanowires and Nanorings Through Oriented Attachment of Nanoparticles. *J. Am. Chem. Soc.* **2005**, *127*, 7140–7147.
34. Hanrath, T.; Veldman, D.; Choi, J. J.; Christova, C. G.; Wienk, M. M.; Janssen, R. A. J. PbSe Nanocrystal Network Formation during Pyridine Ligand Displacement. *ACS. Appl. Mater. Inter.* **2009**, *1*, 244–250.
35. Huis, M. A. v.; Kunneman, L. T.; Overgaag, K.; Xu, Q.; Pandraug, G.; Zandbergen, H. W.; Vanmaekelbergh, D. Low-Temperature Nanocrystal Unification through Rotations and Relaxations Probed by *in Situ* Transmission Electron Microscopy. *Nano Lett.* **2008**, *8*, 3539–3963.
36. PbSe thin films were provided by Jan Koenig; Fraunhofer Institute for Physical Measurement Techniques IPM, G.
37. Cerny, R.; Prikryl, P.; El-Kader, K. M. A.; Chah, V. Determination of the Reflectivity of Liquid Semiconductors over a Wide Temperature Range. *Int. J. Thermophys.* **1995**, *16*, 841–849.
38. Gatskevich, E.; Ivlev, G.; Prikryl, P.; Cerny, R.; Chab, V.; Cibulka, O. Pulser Laser-Induced Phase Transformations in CdTe Single Crystals. *Appl. Surf. Sci.* **2005**, *248*, 259–263.
39. Boneberg, J.; Yavas, O.; Mierswa, B.; Leiderer, P. Optical Reflectivity of Si above the Melting Point. *Phys. Status Solidi (b)* **2006**, *174*, 295–300.
40. Goldstein, A. N.; Echer, C. M.; Alivisatos, A. P. Melting in Semiconductor Nanocrystals. *Science* **1992**, *256*, 1425–1427.
41. Farrell, H. H.; Siclen, C. D. V. Binding Energy, Vapor Pressure, and Melting Point of Semiconductor Nanoparticles. *J. Vac. Sci. Technol. B* **2007**, *25*, 1441–1447.
42. Christenson, H. K. Confinement Effects on Freezing and Melting. *J. Phys.-Condens. Mater.* **2001**, *13*, R95–R133.
43. Choi, J. J.; Luria, J.; Hyun, B.-R.; Bartnik, A. C.; Sun, L.; Lim, Y.-F.; Marohn, J. A.; Wise, F. W.; Hanrath, T. Photogenerated Exciton Dissociation in Highly Coupled Lead Salt Nanocrystal Assemblies. *Nano Lett.* **2010**, *10*, 1805–1811.
44. Yang, C. C.; Armellin, J.; Li, S. Determinants of Thermal Conductivity and Diffusivity in Nanostructural Semiconductors. *J. Phys. Chem. B* **2008**, *112*, 1482–1486.
45. Humphrey, T. E.; Linke, H. Reversible Thermoelectric Nanomaterials. *Phys. Rev. Lett.* **2005**, *94*, 096601.
46. Woochul Kim; Wang, R.; Majumdar, A. Nanostructuring Expands Thermal Limits. *Nano Today* **2007**, *2*, 40–47.
47. Prasher, R. Ultralow Thermal Conductivity of a Packed Bed of Crystalline Nanoparticles: A Theoretical Study. *Phys. Rev. B* **2006**, *74*, 165413–165418.
48. Goodfellow, B. W.; Patel, R. N.; Panthani, M. G.; Smilgies, D.-M.; Korgel, B. A. Melting and Sintering of a Body-Centered Cubic Superlattice of PbSe Nanocrystals Followed by Small Angle X-ray Scattering. *J. Phys. Chem. C* **2011**, *115*, 6397–6404.
49. Wolcott, A.; Doyeux, V; Nelson, C. A.; Gearba, R.; Wai Lei, K. W.; Yager, K. G.; Dolocan, A. D.; Williams, K.; Nguyen, D.; Zhu, X. Y. Anomalously Large Polarization Effect Responsible for Excitonic Red Shifts in PbSe Quantum Dot Solids. *J. Phys. Chem. Lett.* **2011**, *2*, 795–800.
50. Koole, R.; Liljeroth, P.; Donega, C. de M.; Vanmaekelbergh, D.; Meijerink, A. Electronic Coupling and Exciton Energy Transfer in CdTe Quantum-Dot Molecules. *J. Am. Chem. Soc.* **2006**, *128*, 10436–10441.
51. Williams, K. J.; Tisdale, W. A.; Leschkies, K. S.; Haugstad, G.; Norris, D. J.; Aydil, E. S.; Zhu, X. Y. Strong Electronic Coupling in Two-Dimensional Assemblies of Colloidal PbSe Quantum Dots. *ACS Nano* **2009**, *3*, 1532–1538.
52. Yu, W. W. F.; J., C.; Shih, B. S.; Colvin, V. L. Preparation and Characterization of Monodisperse PbSe Semiconductor Nanocrystals in a Noncoordinating Solvent. *Chem. Mater.* **2004**, *16*, 3318–3322.